1 **Improving Madden–Julian Oscillation Simulation in Atmospheric General**

2 **Circulation Models by Coupling with Snow–Ice–Thermocline One-dimensional**

3 **Ocean Model**

4 Wan-Ling Tseng[1,2], Huang-Hsiung Hsu[2*], Yung-Yao Lan[2], Wei-Liang Lee[2], Chia-Ying

5 Tu[2], Pei-Hsuan Kuo[3], Ben-Jei Tsuang[4], Hsin-Chien Liang[2]

6

7 [1]International Degree Program in Climate Change and Sustainable Development,

8 National Taiwan University, Taipei, Taiwan

9 [2]Research Center for Environmental Changes, Academia Sinica, Taipei, Taiwan

10 [3]Center Weather Bureau, Taipei, Taiwan.

11 [4]National Chung-Hsing University, Taichung, Taiwan.

12 Corresponding author: Huang-Hsiung Hsu (hhhsu@gate.sinica.edu.tw)

13

Abstract

A one-column turbulent kinetic energy-type ocean mixed-layer model snow–ice–thermocline (SIT) when coupled with three atmospheric general circulation models (AGCMs) yield superior Madden–Julian Oscillation (MJO) simulation. SIT is designed to have fine layers similar to those observed near the ocean surface; therefore, it can realistically simulate the diurnal warm layer and cool skin. This refined discretization of the near ocean surface in SIT provides accurate sea surface temperature (SST) simulation; thus, facilitating realistic air–sea interaction. Coupling SIT with European Centre Hamburg Model, Version 5, Community Atmosphere Model, Version 5, High-Resolution Atmospheric Model significantly improved MJO simulation in three coupled AGCMs compared with the AGCM driven with prescribed SST. This study suggests two major improvements to the coupling process. First, during the preconditioning phase of MJO over the Maritime Continent (MC), the over underestimated surface latent heat bias in AGCMs can be corrected. Second, during the phase of strongest convection over MC, the change in intraseasonal circulation in the meridional circulation enhancing near-surface moisture convergence is the dominant factor in the coupled simulations relative to the uncoupled experiments. The study results show that a fine vertical resolution near the surface, which better captures temperature variations in the upper few meters of the ocean, considerably improves different models with different configurations and physical parameterization schemes; this could be an essential factor for accurate MJO simulation.

Keywords: Madden–Julian Oscillation, coupling, warm layer

36 **Short summary (plain text)**

37   We show that coupling a high-resolution one-column ocean model to three

38   atmospheric general circulation models dramatically improves Madden–Julian

39   Oscillation (MJO) simulations. It suggests two major improvements to the coupling

40   process in the preconditioning and strongest convection phases over the Maritime

41   Continent. Our results demonstrate a simple but effective way to significantly improve

42   MJO simulation and potentially seasonal to subseasonal prediction.

43

44

1 Introduction

The Madden–Julian Oscillation (MJO) is the dominant pattern of atmospheric intraseasonal variability in the tropics (Madden and Julian, 1972; Zhang, 2005; Jiang et al., 2020). It has been reported that the MJO convection is often observed over sea surface temperature (SST) of greater than 28°C in the Indo-Pacific warm pool (Salby and Hendon, 1994). MJO is an eastward-propagating ocean–atmosphere and convection-circulation coupled phenomenon that lasts for 20–100 days. On these timescales, low-level moisture convergence, warm SST, and shallow upper-ocean mixed-layer depth precede the eastward propagation of organized deep convection by approximately ten days; opposite conditions followed by approximately ten days (Krishnamurti et al., 1988; Hendon and Salby, 1994; Woolnough et al., 2000). Heat flux exchange between the atmosphere and ocean modulates the intraseasonal oscillation (Shinoda and Hendon, 1998). Studies have emphasized the importance of moisture and heat flux feedback in MJO (Sobel et al., 2008, 2010; DeMott et al., 2015). Besides, oceanic wave dynamics are suggested to be associated with MJO, for example, zonal wind stress anomalies driven by the MJO force eastward-propagating oceanic equatorial Kelvin wave (Hendon et al., 1998; Webber et al., 2010), and the signals could extend as deep as 1500 m in the ocean (Matthews et al., 2007). Furthermore, the westward-propagating oceanic equatorial Rossby wave can initiate the next MJO in the Indian Ocean (Webber et al., 2010; Webber et al., 2012). Evidence of oceanic intraseasonal signals coupling with atmospheric signals was observed in terms of the sea level, surface heat flux, salinity, and temperature during field experiments and in situ monitoring (Oliver and Thompson, 2011; Drushka et al., 2012; Wang et al., 2013; Chi et al., 2014; Matthews et al., 2014; DeMott et al., 2015; Fu et al., 2015).

69   Recent modeling studies have demonstrated that most coupled models could

70   improve MJO simulations but that the ocean driven by the atmosphere contributes

71   indirectly by improving the mean state, heat flux, fresh water, and momentum. DeMott

72   et al. (2016) estimated that direct SST-driven ocean feedback contributes to the MJO

73   propagation up to 10% by a change in column moisture. A comparison of the direct and

74   indirect effects of SST indicated that direct effects, such as SST-driven surface fluxes,

75   tend to offset wind-driven fluxes (DeMott et al., 2015; DeMott et al., 2016; DeMott et al.,

76   2019). The factor of indirect ocean feedback on the atmospheric physical process includes

77   strong MJO convection can amplify the radiative feedback to MJO convections

78   associated with large cloud systems (Del Genio and Chen, 2015). The SST gradients can

79   dive the MJO low-level convergence (Hsu and Li, 2012; Li and Carbone, 2012) and

80   destabilize lower tropospheric to further enhance low-level convergence to the east of

81   MJO convergence (Wang and Xie, 1998; Marshall et al., 2008; Benedict and Randall,

82   2011; Fu et al., 2015). Many observational and model studies have reported that coupled

83   feedback enhances the MJO with strong horizontal moisture advection, driven by sharp

84   mean near-equatorial meridional moisture gradients (DeMott et al., 2015; Jiang et al.,

85   2018; DeMott et al., 2019; Jiang et al., 2020). These findings suggest that high-frequency

86   SST perturbations could improve moisture convergence efficiency and enhance MJO

87   propagation through relatively smooth background moisture distribution.

88   Tseng et al. (2015) identified the key role of the upper-ocean warm layer in

89   improving the MJO eastward propagation simulation using the European Centre

90   Hamburg Model, Version 5 (ECHAM5), coupled with the one-column ocean model

91   named snow–ice–thermocline (SIT). Many observational (Drushka et al., 2012; Chi et al.,

92   2014) and modeling (Klingaman and Woolnough, 2013; DeMott et al., 2019; Klingaman

93   and Demott, 2020) studies have supported this hypothesis. However, coupling the SIT to

94   only one atmospheric general circulation model (AGCM) may be insufficient to prove

95   the effectiveness of the coupling. In this study, we coupled the SIT to three AGCMs:

96   ECHAM5, Community Atmosphere Model, Version 5 (CAM5), and High-Resolution

97   Atmospheric Model (HiRAM). We also discussed the coupling mechanism that leads to

98   simulation improvement.

99   The remainder of the paper is organized as follows. In section 2, we describe the

100   models, experimental designs, and observational data. Section 3 and 4 present the results

101   and discussion, respectively.

102   **2 Data, model experiments and methodology**

103   **2.1 Observation and atmospheric/oceanic data**

104   Observational data used in this study include precipitation from Global Precipitation

105   Climatology Project V1.3 (GPCP, 1° resolution, 1997–2010; Adler et al., 2003), outgoing

106   longwave radiation (OLR, 1° resolution, 1997–2010; Liebmann, 1996) and daily SST

107   (Optimum Interpolated SST, 0.25° resolution, 1989–2010; Banzon et al., 2014) from the

108   National Oceanic Atmosphere Administration. The in situ ocean temperature profiles

109   from 1989 to 2010 were obtained from the Tropical Ocean Global Atmosphere program

110   (McPhaden et al., 2010).

111   Atmospheric variables were obtained from the European Centre for Medium-range

112   Weather Forecast Reanalysis-interim (Dee et al., 2011) from 1989 to 2010. The variables

113   include zonal wind, meridional wind, temperature, specific humidity, sea level pressure,

114   geopotential high, latent heat, sensible heat, shortwave and longwave radiation. Oceanic

115 temperature data from 1989 to 2010 were obtained from the NCEP Global Ocean Data

116 Assimilation System (GODAS) (Behringer and Xue, 2004) provided by the

117 NOAA/OAR/ESRL PSL, Boulder, Colorado, USA

118 (https://psl.noaa.gov/data/gridded/data.godas.html).

119 **2.2 Model experiments**

120 In this study, we coupled the one-column ocean model SIT (Tu and Tsuang, 2005;

121 Tsuang et al., 2009) to three AGCMs. SIT simulates variations in the SST and upper-

122 ocean temperature, including the diurnally-varying cool skin and warm layer in the upper

123 few meters of the ocean and the turbulent kinetic energy (TKE; Gaspar et al., 1990) in

124 the water column (Tsuang et al., 2001; Tu and Tsuang, 2005; Tu, 2006; Tsuang et al.,

125 2009; Tu and Tsuang, 2014; Tseng et al., 2015; Lan et al., 2021). Cool skin is a very thin

126 layer that has a direct contact with the atmosphere and warm layer is the warmer sea water

127 immediately below the cool skin in the top few meters of the ocean. They fluctuate

128 diurnally in response to atmospheric forcing. SIT with high vertical resolution

129 realistically simulates the warm-layer (within top 10 m) and cool-skin (the top layer with

130 0.001 m thickness), and improve the simulation of upper ocean temperature (Tu and

131 Tsuang, 2005; Tsuang et al., 2009). The model has been verified at a tropical ocean site

132 (Tu and Tsuang, 2005), in the South China Sea (Lan et al., 2010), and Caspian Sea

133 (Tsuang et al., 2001). The melt and formation of snow and ice above a water column have

134 been introduced (Tsuang et al., 2001). The three AGCMs used in this study are as follows.

135 ECHAM5, the fifth-generation AGCM developed at the Max Planck Institute for

136 Meteorology (Roeckner, 2003; Roeckner et al., 2006) is a spectral model that employs

137 the Nordeng (Nordeng, 1994) cumulus convective scheme. We used a horizontal

138 resolution of T63 (approximately 2°) with 31 vertical layers and a model top at 10 hPa

139 (approximately 30 km). The second one is NCAR Community Atmospheric Model

140 version 5 (Hurrell et al., 2013) from the National Center for Atmospheric Research. We

141 used a horizontal resolution of approximately 1.875° latitude × 2.5° longitude and 30

142 vertical layers with the Zhang–McFarlane deterministic convection scheme (Zhang and

143 McFarlane, 1995) and the University of Washington Shallow Convection (Park and

144 Bretherton, 2009). HiRAM was developed based on Geophysical Fluid Dynamical

145 Laboratory global atmosphere and land model AM2 (Team et al., 2004; Zhao et al., 2009)

146 with few modifications (Chen et al., 2019). We used a horizontal resolution of

147 0.5° latitude × 0.5° longitude with 32 vertical levels. For boundary layer and free

148 atmospheric turbulence, the model adopted the 2.5 order parameterization of Mellor and

149 Yamada (1982). Surface fluxes are computed based on the Monin–Obukhov similarity

150 theory, given the atmospheric model's lowest level of wind, temperature, and moisture.

151   There are 42 vertical layers in SIT, with 12 layers in the upper 10 m: the surface,

152 0.05 mm, 1 m, 2 m, 3 m, 4 m, 5 m, 6 m, 7 m, 8 m, 9 m, and 10 m below ocean surface.

153 The fine resolution was designed to realistically simulate the upper-ocean warm layer,

154 including a layer at 0.05 mm, reproducing the cool skin of the ocean surface. It is worth

155 noting that coupling a high-vertical-resolution TKE ocean model with an AGCM is

156 unconventional. To account for neglected horizontal processes, the model ocean was

157 weakly nudged (with a 30-day time scale) to the observed GODAS monthly mean ocean

158 temperature below a depth of 10 m. Nudging was not applied in the upper 10 m. The

159 timestep of SIT and AGCMs exchange ocean surface fluxes varying associated with the

160 model resolution, which is 720, 1800, and 900 seconds in ECHAM-SIT, CAM5-SIT, and

161 HiRAM-SIT, respectively. AGCMs were coupled with the SIT in the tropical region

162 between 30°S and 30°N and forced by prescribed monthly mean OISST outside this

163 tropical belt.

164   The experiments comprised three sets of coupled AGCM simulations (ECHAM5-

165 SIT, CAM5-SIT, and HiRAM-SIT) and standalone AGCM simulations forced by

166 observed monthly mean OISST (ECHAM5, CAM5, and HiRAM) from 1985 to 2005.

167 The experiments were designed to evaluate the effect of atmosphere–ocean coupling on

168 MJO simulations. Table 1 presents the model and experiment details.

169   **2.3 Methodology**

170   The analysis focused on the boreal cool season (November–April) when the

171 eastward propagation tendency of the MJO is the most prominent. We used the CLIVAR

172 MJO Working Group diagnostics package (CLIVAR, 2009) and a 20–100-day filter to

173 analyze intraseasonal variability. The MJO phase composites were computed using the

174 real-time multivariate MJO index (Wheeler and Hendon, 2004), defined as the leading

175 pair of principal components of intraseasonal OLR, and 850 and 200 hPa zonal winds in

176 the tropics.

177   The vertically integrated MSE budget was diagnosed based on the following

178 equation:

179 $\left\langle \frac{\partial h}{\partial t} \right\rangle' = -\left\langle u\frac{\partial h}{\partial x} \right\rangle' - \left\langle v\frac{\partial h}{\partial y} \right\rangle' - \left\langle \omega\frac{\partial h}{\partial p} \right\rangle' + \langle LW \rangle' + \langle SW \rangle' + \langle LH \rangle' + \langle SH \rangle'$ (1)

180 where h is the MSE ($h = cpT + gz + Lq$); u and v are the zonal and meridional velocities,

181 respectively; ω is the vertical pressure velocity; LW and SW are the longwave and

182 shortwave radiation fluxes, respectively; LH and SH are the latent and sensible surface

183 heat fluxes, respectively. The mass–weighted vertical integration from the surface to 200

184 hPa is denoted as $\langle \cdot \rangle$, and intraseasonal anomalies are represented as $\langle \cdot \rangle'$, which were

185 isolated using a 20–100-day bandpass Lanczos filter (Duchon, 1979).

186

3 Results

3.1 MJO simulations: ECHAM5-SIT, CAM5-SIT, and HiRAM-SIT

3.1.1 General structure

190   We compared simulated MJO characteristics using three coupled and uncoupled

191 AGCMs. Figure 1 shows the wavenumber–frequency spectra of simulated 850-hPa zonal

192 wind (shading) and precipitation (contours). All three uncoupled AGCMs (hereafter

193 referred to as AGCMs) simulated intraseasonal signals with lower frequency than the

194 observed and overestimated the westward propagation with periods greater than 80 days

195 (Figs. 1e–g). The ECHAM5 and HiRAM simulated signals of wavenumbers 1–3 instead

196 of the observed wavenumber 1 in 850-hPa zonal wind. These results show that all three

197 AGCMs simulated stationary fluctuations with low frequency that were not consistent

198 with the observation. By contrast, coupled AGCMs realistically reproduce the observed

199 spectral characteristics and strength of the eastward propagation at wavenumbers 1 to 2

200 in 850-hPa zonal wind (Figs. 1b–d). Although HiRAM simulated eastward propagation

201 in a wider frequency spectrum than the observed, the coupled model clearly displays

202 improvements in the MJO simulation compared with the stationary intraseasonal

203 fluctuation in the uncoupled simulation. Hovmöller diagrams presented in Fig. 2 illustrate

204 the temporal evolution of 850-hPa zonal wind and precipitation in the tropics in

205 observation and simulations. All three models simulated either stationary (CAM5 and

206 HiRAM) or weak eastward-propagating (ECHAM5) signals in AGCMs, but more

207 realistically simulated the eastward propagation of the MJO in the coupled models.

208   However, the propagation in the ECHAM5-SIT is still slightly slower than the observed.

209   The improvement obtained in coupled models suggests that active ocean–atmosphere

210   interaction is crucial for successful MJO simulation.

211   **3.1.2 Atmospheric and oceanic profiles**

212   The composite MJO life cycle featuring intraseasonal OLR and 10-m surface wind

213   anomalies for boreal winter in eight phases following Wheeler and Hendon (2004) is

214   displayed in Fig. 3. All three coupled models simulated realistic MJO with enhanced

215   circulations and propagation tendency compared with the uncoupled ones. The MJO in

216   phase 4, when deep convection is the strongest over the Maritime Continent (MC),

217   demonstrates the large-scale zonally overturning circulation coupling with the convection

218   (Fig. 4). The positive heating region in the coupled experiment is significantly enlarged,

219   deepened, and westward-tilted with increasing height compared with those in the

220   uncoupled experiment. Correspondingly, the convective-circulation envelope of the MJO

221   is thicker and longitudinally wider in coupled experiments. The strong convection is

222   associated with much enhanced low-level moisture convergence (green contours).

223   Furthermore, the area of positive rainfall anomaly in the coupled experiment becomes

224   larger, and the sea level pressure anomaly is meridionally more confined, exhibiting the

225   characteristics of intensified Kelvin wave-like perturbations to the east of the deep

226   convection. This enhancement of low-level moisture convergence is consistent with the

227   frictional wave-conditional instability of the second kind mechanism (Wang and Rui,

228   1990; Kang et al., 2013). The enhancement of the Kelvin wave can be observed in the

229   symmetric wavenumber–frequency spectra (Fig. 5). The spectra between 0 and 0.35 day^{-1}

230   are presented to highlight the MJO and equatorial Kelvin waves. The coherence at

231   wavenumbers of 2–4 for the 10–20-day period is simulated stronger in three coupled than

232   uncoupled models.

233   In addition to the atmospheric structure, the SST (Fig. S1) and vertical profile of

234   ocean temperature examined are presented in Fig. 6. The observed SST variation in MJO

235   variability is well reproduced in all three coupled models (Fig. S1). The warm SST leads

236   the main MJO convection by approximately 5–10 days, followed by the cold SST

237   approximately 5–10 days later (Flatau et al., 1997; DeMott et al., 2015; Tseng et al., 2015).

238   Moreover, the observed amplitude fluctuation (approximately 0.5° to 1°C) is realistically

239   simulated. The observed ocean temperature profiles, characterized by the warm layer,

240   along the equator from the Indian Ocean to the western Pacific are well simulated in the

241   three coupled models (Fig. 6). Meanwhile, simulated temperature anomalies are larger in

242   ECHAM5-SIT than in CAM5-SIT and HiRAM-SIT. Figure. S2 shows the fluctuations of

243   observed SST and simulated SST in three sets of coupled and uncoupled model. There is

244   no fluctuation as expected in uncoupled simulations, whereas the simulated SST

245   fluctuates with phases similar to the observed at different locations. The amplitudes in

246   ECHAM5-SIT and CAM5-SIT are similar to the observed, whereas those in HiRAM-SIT

247   seems to be smaller in the western Pacific. The differences between models are likely due

248   to the different atmospheric model configurations, because they were coupled to the same

249   1-D ocean model. Since the atmosphere is the main driver to extract heat form the ocean,

250   different responses of atmospheric models likely have different effects on SST. The cause

251   of quantitative differences between models needs further detailed analysis to pinpoint.

252   The consistent results in all three coupled models support the conclusion of Tseng et al.

253   (2015) that resolving fine vertical resolution in the upper ocean improves the simulation

254   of the warm layer and MJO propagation and variability. Our results further demonstrate

255   that the effect of atmosphere–ocean coupling on the MJO could be independent of

256   AGCMs with different configurations and atmospheric physical parameterizations, and

257   that coupling seems to be a more fundamental approach.

258 3.1.3 Performance comparison

259   Model performance is summarized in Fig. 7. The scatter plot shows the power ratio

260   of east–west propagating waves (X-axis) versus the pattern correlation between the

261   simulated and observed precipitation anomaly in Hovmöller diagrams (Fig. 2; Y-axis).

262   The east:west ratio was calculated by dividing eastward-propagating power by westward-

263   propagating power of 850–hPa zonal wind summed over wavenumbers of 1–2 and a

264   period of 30–80 days. Compared with the observation, coupled simulations (marked by

265   circles) exhibit better simulation than uncoupled simulations (marked by asterisks). A

266   comparison of combined explained variance using RMM1 and RMM2 (Fig. 7b) based on

267   Wheeler and Hendon (2004) shows marked increases after coupling. The comparison

268   demonstrates that coupling is essential for realistic MJO simulations.

269 3.2 Mechanism discussion

270   We applied the MSE budget to diagnose the moisture budget associated with the

271   MJO. Figure 8 shows a Hovmöller diagram of MSE tendency averaged by 10°S–EQ

272   overlaying precipitation anomalies. MSE tendency derived from reanalysis fluctuates in

273   quadrature with precipitation anomaly with positive (negative) MSE tendency, leading

274   (lagging) major convection by approximately one to two phases (DeMott et al., 2015;

275   DeMott et al., 2016; DeMott et al., 2019). Coupled models simulate stronger eastward

276   propagation in the MSE tendency and precipitation anomalies and realistic phase lag

277   between the two. Stronger MSE tendencies in coupled simulations are observed in

278   ECHAM5 and HiRAM but are less clear in CAM5. Figures 8d, g, and j show the

279   differences between coupled and uncoupled simulations. One notable feature is the

280   positive (negative) MSE tendency preceding positive (negative) precipitation anomaly

281   and preconditions an environment for eastward propagation of active (inactive)

282   convection and associated circulation. Next, we diagnosed the relative contribution of

283   each term in Equation 1 to the MSE tendency with the focus on the MC, where the largest

284   positive MSE tendency and precipitation anomaly were found.

285   **3.2.1 Preconditioning phase**

286   Following the peak MSE tendency over the MC (120°E–150°E) during phase 2 (Figs.

287   8d, g, and j), values of each term contributing to the column-integrated MSE tendency in

288   Equation 1 preceding the deep convection over the MC area (10°S–EQ, 120°E–150°E)

289   are shown in Fig. 9. Vertical advection is the dominant term with the major compensation

290   from longwave radiation during phase 2 when convection is still in the eastern Indian

291   Ocean, as identified by Wang et al. (2017). Moreover, the LH term is consistent within

292   all three models to contribute less negative MSE tendency in coupled models than

293   ACGMs. The results show that the contribution comes from the LH term in this early

294   phase stage. The LH effect was overlooked in Tseng et al. (2015) because of the weak

295   MJO variability in coupled simulations. However, this negative LH bias becomes one of

296   the key factors in enhancing the leading MSE tendency during the MJO preconditioning

297   phases. This suggests that the surface latent flux bias in AGCMs can be corrected by

298   involving the coupling process in the preconditioning phase. Generally, coupling

299   improves the budget simulation. The positive contribution of vertical advection and

300   negative contribution of LH in MSE tendency is closer to realistic in the coupled

301   simulations during the initial phase of the MJO.

302   **3.2.2 Phase of strongest convection over MC**

303   We compared the spatial distribution of MSE and precipitation in phase 4 when

304   convection was the strongest in the MC (Fig. 10). In the observation, the main convection

305   occurs in the MC from 90°E to 150°E. A positive MSE tendency with a maximum value

306   near 10°N and 10°S is identified in the east of the MJO convection centered near the

307   equator. Meanwhile, a negative integrated MSE tendency is found in the west of the MJO

308   convection, and the meridionally confined structure near the equator exhibits the

309   characteristics of the equatorial Kelvin wave embedded in the MJO. Clearly, coupled

310   models outperform uncoupled models in reproducing these signals. To quantify the

311   contribution of coupling to the improvement, we follow Jiang et al. (2018) to project all

312   MSE terms to the observations (Fig. 11). The dominant contribution of horizontal

313   advection to the MSE tendency in observation (Fig. 11a) is well simulated in the coupled

314   simulations but not in uncoupled simulations by ECHAM5 and CAM5 (Figs. 11b and c).

315   Although a similar dominant effect was observed in both simulation types in HiRAM, it

316   is enhanced in the coupled simulation (Fig. 11d). The horizontal advection term is further

317   decomposed into zonal and meridional components (Figs. 11e–h); both components have

318   a positive contribution, but the meridional component has a larger amplitude.

319   Furthermore, the uncoupled ECHAM5 and CAM5 simulate unrealistic features: positive

320   contribution from zonal advection but negative contribution from meridional advection.

321   In contrast, coupled models well simulate the dominance of meridional advection. In

322   HiRAM, the uncoupled model simulates almost equally positive contributions from both

323   terms. However, the coupled model simulates a larger contribution from meridional

324   advection. We further decompose the meridional advection to assess the relative

325   contributions of an intraseasonal perturbation and the mean state. Consistent with the

326   observations (Fig. 11i), the meridional advection by intraseasonal flow ($-v'\frac{\partial \overline{h}}{\partial y}$) is the

327   main factor in improving the simulations in the coupled models (Figs. 11j–l). Our results

328   are consistent with those of Jiang et al. (2018). To evaluate the relative contribution of

329   intraseasonal circulation and background moisture, we further diagnosed changes in

330    $\Delta(-v'\frac{\partial \overline{h}}{\partial y})$ at phase 4. Here the overbar shows that the time mean and prime represents

331   intraseasonal anomaly. Changes in the MJO meridional advection term for coupled

332   experiments relative to uncoupled can be written as follows:

$$333 \quad \Delta\left(-v'\frac{\partial \overline{m}}{\partial y}\right) = -\Delta v'\left(\frac{\partial \overline{m}}{\partial y}\right)_{uncoupled} - \left(v'\right)_{uncoupled}\Delta\left(\frac{\partial \overline{m}}{\partial y}\right) - \Delta v'\Delta\left(\frac{\partial \overline{m}}{\partial y}\right) \ (2)$$

334   (a) (b) (c)

335   where Δ represents the coupled–uncoupled change. The terms a–c are presented as bar

336   charts in Fig. 12. The change of the intraseasonal circulation in the meridional circulation

337   is the dominant factor in coupled simulations relative to uncoupled experiments. The

338   instantaneous SST horizontal distribution dominates this moisture budget change due to

339   the atmosphere–ocean coupling effect. Therefore, the change of varying moisture induces

340   the intraseasonal circulation change. The results confirm that the dominance of dynamic

341   influence over thermodynamic response to atmosphere–ocean coupling is essential in

342   improving MJO simulations.

3.3 Discussion: mean state and intraseasonal variance

We examined the simulated mean state, which has been suggested a key factor affecting MJO simulations (Inness et al., 2003; Watterson and Syktus, 2007; Kim et al., 2009; Kim et al., 2011; Kim et al., 2014; Jiang et al., 2018; Jiang et al., 2020). The three models exhibited different tropical SST responses to coupling (Fig. S3e). Over the warm pool area, CAM-SIT and HiRAM-SIT underestimate the SST, whereas ECHAM5-SIT overestimates the SST. Note that warm SST bias in the eastern tropical Pacific was simulated in the three models due to the lack of oceanic circulation in the SIT. The simulated zonal wind in the three models (Figs. S3b–d) demonstrated different responses to coupling. Figures S2c show the 850-hPa zonal wind differences between coupled and uncoupled models (shading) and the total field in uncoupled models (contours). Figures S3f–h show the 10°S–EQ averaged 850-hPa zonal in the coupled and uncoupled models. In ECHAM5-SIT, the westerly wind is slightly enhanced in the eastern Indian Ocean but decreases in the western Indian Ocean and western Pacific. In CAM5-SIT, westerly wind reduces in the Indian Ocean but enhances over the western Pacific. The HiRAM-SIT has similar changes as in ECHAM5-SIT, e.g., decreases over the MC area but increases in the western Indian Ocean and Pacific. Generally, the three models disagree on the zonal wind mean state changes in response to coupling.

The mean moisture changes are substantially enhanced over the tropical areas in ECHAM5 after coupling (Figs. S4b and e). However, in CAM5 and HiRAM, no clear change was observed to the south of the equator, but strong drying was observed to in the north (Figs. S4c, d, f, and g). The only common feature among the three models e is the enhanced meridional gradient of mean moisture, which is consistent with many previous studies (Kim et al., 2014; Jiang et al., 2018; Ahn et al., 2020). Our budget analysis

367 demonstrated that the meridional transport by the intraseasonal meridional circulation is

368 the dominant term. It also showed that the meridional gradient of mean moisture is the

369 secondary effect in enhancing MJO simulations by coupling. After coupling, the mean

370 precipitation changes are more consistent among the three models (Fig. S5). One of the

371 major changes is the southward shift of the major precipitation zone, resulting in

372 precipitation increases over the regions south of the equator, except in the MC. Similarly,

373 the precipitation intraseasonal variance (20–100 days filtered) was markedly enhanced in

374 these regions (Fig. S6). The ECHAM5-SIT exhibits a relatively minor increase over the

375 western MC. In contrast, the HiRAM-SIT exhibits the strongest enhancement,

376 particularly in the Indian Ocean. Generally, all three coupled models enhance the

377 intraseasonal signals over the tropics with discrepancies in detail. Meanwhile, the model

378 mean state does not substantially improve after coupling. Thus, in this study, the mean

379 state is not the main contribution to enhancing the MJO simulation after coupling. Instead,

380 coupling leading to rigorous atmosphere–ocean interaction in intraseasonal time scale is

381 likely the reason for improving MJO simulation.

382

383 **4 Discussion**

384   This study used a one-column TKE-type ocean mixed-layer model SIT coupled

385 with AGCMs to improve MJO simulation. SIT that is designed to have fine layers near

386 the surface well simulates warm layer, cool skin, and their diurnal fluctuations. This

387 refined discretization under the ocean surface in SIT provides improved SST simulation;

388 thus, improving realistic air–sea interaction. Coupling SIT with ECHAM5, CAM5, and

389 HiRAM significantly improves the MJO simulation in the three AGCMs compared with

390 that in the prescribed SST-driven AGCMs. The vertical cross-section indicates that the

391   strengthened low-level convergence during the preconditioning phase is better simulated

392   in the coupled experiment. Furthermore, the phase variation and amplitude of the SST

393   and ocean temperature under the surface can be realistically simulated. Our results reveal

394   that the MJO can be realistically simulated in terms of strength, period, and propagation

395   speed by increasing the vertical resolution of the one-column ocean model to better

396   resolve the upper-ocean warm layer.

397   The MSE budget analysis revealed that the coupling effects during the

398   preconditioning and mature phases exhibit different contributions. During the

399   preconditioning phase, the positive contribution of vertical advection and negative

400   contribution of LH in MSE tendency are closer to realistic values in coupled simulations

401   during the initial phase of the MJO. Additionally, the meridional component of the

402   horizontal advection term is the dominant term during the mature phase of the strongest

403   convection in the MC to enhance the simulation after coupling. Improved meridional

404   circulation is essential in the coupled simulations that outperformed uncoupled

405   experiments. The results confirm that the dominance of dynamic influence over

406   thermodynamic influence in response to the atmosphere–ocean coupling is the key

407   process in improving MJO simulations.

408   In summary, this study suggests two major enhancements of the coupling process.

409   First, the underestimated surface LH bias in AGCMs can be corrected during the

410   preconditioning phase of the MJO over MC. Second, during the strongest convection

411   phase over MC, the change in intraseasonal circulation in the meridional circulation is the

412   dominant factor in coupled simulations relative to uncoupled experiments. Although

413   many studies have indicated the key role played by the mean state, the mean state in our

414 simulations provides only a secondary contribution to enhancing MJO simulation, with

415 coupling being the main contributor. For example, zonal wind and precipitation changed

416 inconsistently among the three models after coupling. Instead, the meridional gradient of

417 the mean moisture and intraseasonal precipitation variance has a better relationship after

418 coupling. Therefore, coupling leading to rigorous atmosphere–ocean interaction in the

419 intraseasonal time scale, but no change in mean states, is likely the reason for MJO

420 simulation improvement. This study supports previous findings (Tseng et al., 2015) that

421 enhancing atmosphere–ocean coupling by considering an extremely high vertical

422 resolution in the first few meters of the ocean model improves MJO simulations. It also

423 supports that this improvement is independent of AGCMs with different configurations

424 and physical parameterization schemes. Resolving the atmosphere–ocean coupling may

425 be more beneficial than modifying the atmospheric physical parameterization schemes in

426 GCM. In brief, this study suggested the effectiveness of air–sea coupling for improving

427 MJO simulation in a climate model and demonstrated the critical effect of being able to

428 simulate warm layer. Additionally, the findings presented here enhance our understanding

429 of the physical processes that shape the characteristics of the MJO.

430

431   **Code and data availability.** The model code of CAM5–SIT, ECHAM5-SIT and

432   HiRAM-SIT   is   available   at   https://doi.org/10.5281/zenodo.5701538,

433   https://doi.org/10.5281/zenodo.5510795   and   https://doi.org/10.5281/zenodo.5701579.

434   Observational data used in this study include precipitation from Global Precipitation

435   Climatology Project V1.3 (GPCP, 1° resolution), OLR (1° resolution), and daily SST

436   (Optimum Interpolated SST, 0.25° resolution) from the National Oceanic and

437   Atmosphere Administration, and variables were obtained from the European Centre for

438   Medium-range Weather Forecast Reanalysis-interim. All experiments were conducted at

439   the National Center for High-performance Computing. All model codes and data

440   availability presented here can be obtained by contacting the first author, Dr. Wan-Ling

441   Tseng (wtseng@ntu.edu.tw).

442

443   **Author contributions.** HHH and WLT have responsibility for conceptualization,

444   including analyzing the data and writing the manuscript. YYL, WLL, PHK, BJT, CYT,

445   and HCL developed the model and provided the simulations.

446

447   **Competing interests.** The authors declare that they have no conflict of interest.

448

454   for Atmospheric Research and their Atmosphere Model Working Group for release

455   CESM1.2.2. This manuscript was edited by Wallace Academic Editing and Enago.

456

457 **References**

458 Adler, R. F., Huffman, G. J., Chang, A., Ferraro, R., Xie, P.-P., Janowiak, J., Rudolf, B.,

459   Schneider, U., Curtis, S., and Bolvin, D.: The version-2 global precipitation

460   climatology project (GPCP) monthly precipitation analysis (1979-present), Journal

461   of Hydrometeorology, 4, 1147-1167, 2003.

462 Ahn, M. S., Kim, D., Kang, D., Lee, J., Sperber, K. R., Gleckler, P. J., Jiang, X., Ham,

463   Y. G., and Kim, H.: MJO propagation across the Maritime Continent: Are CMIP6

464   models better than CMIP5 models?, Geophysical Research Letters, 47,

465   e2020GL087250, 2020.

466 Banzon, V. F., Reynolds, R. W., Stokes, D., and Xue, Y.: A 1/4-spatial-resolution daily

467   sea surface temperature climatology based on a blended satellite and in situ

468   analysis, Journal of Climate, 27, 8221-8228, 2014.

469 Behringer, D. and Xue, Y.: Evaluation of the global ocean data assimilation system at

470   NCEP: The Pacific Ocean, Proc. Eighth Symp. on Integrated Observing and

471   Assimilation Systems for Atmosphere, Oceans, and Land Surface,

472 Benedict, J. J. and Randall, D. A.: Impacts of Idealized Air–Sea Coupling on Madden–

473   Julian Oscillation Structure in the Superparameterized CAM, Journal of the

474   Atmospheric Sciences, 68, 1990-2008, 10.1175/jas-d-11-04.1, 2011.

475 Chen, C.-A., Hsu, H.-H., Hong, C.-C., Chiu, P.-G., Tu, C.-Y., Lin, S.-J., and Kitoh, A.:

476   Seasonal precipitation change in the western North Pacific and East Asia under

477   global warming in two high-resolution AGCMs, Climate Dynamics, 53, 5583-

478   5605, 2019.

479 Chi, N. H., Lien, R. C., D'Asaro, E. A., and Ma, B. B.: The surface mixed layer heat

480   budget from mooring observations in the central Indian Ocean during Madden–

481   Julian Oscillation events, Journal of Geophysical Research: Oceans, 119, 4638-

482   4652, 2014.

483   CLIVAR, M. J. O. W. G.: MJO Simulation Diagnostics, Journal of Climate, 22, 3006-

484   3030, 2009.

485   Dee, D., Uppala, S., Simmons, A., Berrisford, P., Poli, P., Kobayashi, S., Andrae, U.,

486   Balmaseda, M., Balsamo, G., and Bauer, P.: The ERA-Interim reanalysis:

487   Configuration and performance of the data assimilation system, Quarterly Journal

488   of the Royal Meteorological Society, 137, 553-597, 2011.

489   Del Genio, A. D. and Chen, Y.: Cloud-radiative driving of the Madden-Julian

490   oscillation as seen by the A-Train, Journal of Geophysical Research: Atmospheres,

491   120, 5344-5356, https://doi.org/10.1002/2015JD023278, 2015.

492   DeMott, C. A., Klingaman, N. P., and Woolnough, S. J.: Atmosphere-ocean coupled

493   processes in the Madden-Julian oscillation, Reviews of Geophysics, 53, 1099-

494   1154, 2015.

495   DeMott, C. A., Benedict, J. J., Klingaman, N. P., Woolnough, S. J., and Randall, D. A.:

496   Diagnosing ocean feedbacks to the MJO: SST-modulated surface fluxes and the

497   moist static energy budget, Journal of Geophysical Research: Atmospheres, 121,

498   8350-8373, 2016.

499   DeMott, C. A., Klingaman, N. P., Tseng, W. L., Burt, M. A., Gao, Y., and Randall, D.

500   A.: The convection connection: How ocean feedbacks affect tropical mean

501   moisture and MJO propagation, Journal of Geophysical Research: Atmospheres,

502   124, 11910-11931, 2019.

503   Drushka, K., Sprintall, J., Gille, S. T., and Wijffels, S.: In situ observations of Madden-

504   Julian Oscillation mixed layer dynamics in the Indian and western Pacific Oceans,

505   Journal of Climate, 25, 2306-2328, 2012.

506   Duchon, C. E.: Lanczos filtering in one and two dimensions, Journal of Applied

507   Meteorology and Climatology, 18, 1016-1022, 1979.

508   Flatau, M., Flatau, P. J., Phoebus, P., and Niiler, P. P.: The feedback between equatorial

509   convection and local radiative and evaporative processes: The implications for

510   intraseasonal oscillations, Journal of the atmospheric sciences, 54, 2373-2386,

511   1997.

512   Fu, X., Wang, W., Lee, J.-Y., Wang, B., Kikuchi, K., Xu, J., Li, J., and Weaver, S.:

513   Distinctive roles of air–sea coupling on different MJO events: A new perspective

514   revealed from the DYNAMO/CINDY field campaign, Monthly Weather Review,

515   143, 794-812, 2015.

516   Gaspar, P., Gregoris, Y., and Lefevre, J.-M.: A simple eddy kinetic energy model for

517   simulations of the oceanic vertical mixing: Tests at station Papa and long-term

518   upper ocean study site, Journal of Geophysical Research: Oceans, 95, 16179-

519   16193, 1990.

520   Hendon, H. H. and Salby, M. L.: The life cycle of the Madden-Julian oscillation,

521   Journal of the Atmospheric Sciences, 51, 2225-2237, 1994.

522   Hendon, H. H., Liebmann, B., and Glick, J. D.: Oceanic Kelvin waves and the

523   Madden‐Julian oscillation, Journal of the Atmospheric Sciences, 55, 88-101,

524   1998.

525   Hsu, P.-C. and Li, T.: Role of the Boundary Layer Moisture Asymmetry in Causing the

526   Eastward Propagation of the Madden-Julian Oscillation*, Journal of Climate, 25,

527   4914-4931, 2012.

528   Hurrell, J. W., Holland, M. M., Gent, P. R., Ghan, S., Kay, J. E., Kushner, P. J.,

529   Lamarque, J.-F., Large, W. G., Lawrence, D., and Lindsay, K.: The community

530   earth system model: a framework for collaborative research, Bulletin of the

531   American Meteorological Society, 94, 1339-1360, 2013.

532   Inness, P. M., Slingo, J. M., Guilyardi, E., and Cole, J.: Simulation of the Madden-

533   Julian Oscillation in a coupled general circulation model. Part II: The role of the

534   basic state, Journal of Climate, 16, 365-382, 2003.

535   Jiang, X., Adames, Á. F., Zhao, M., Waliser, D., and Maloney, E.: A unified moisture

536   mode framework for seasonality of the Madden–Julian oscillation, Journal of

537   Climate, 31, 4215-4224, 2018.

538   Jiang, X., Adames, Á. F., Kim, D., Maloney, E. D., Lin, H., Kim, H., Zhang, C.,

539   DeMott, C. A., and Klingaman, N. P.: Fifty years of research on the Madden-Julian

540   Oscillation: Recent progress, challenges, and perspectives, Journal of Geophysical

541   Research: Atmospheres, 125, e2019JD030911, 2020.

542   Kang, I.-S., Liu, F., Ahn, M.-S., Yang, Y.-M., and Wang, B.: The Role of SST Structure

543   in Convectively Coupled Kelvin-Rossby Waves and Its Implications for MJO

544   Formation, Journal of Climate, 26, 5915–5930, 2013.

545   Kim, D., Sobel, A. H., Maloney, E. D., Frierson, D. M., and Kang, I.-S.: A systematic

546   relationship between intraseasonal variability and mean state bias in AGCM

547   simulations, Journal of Climate, 24, 5506-5520, 2011.

548   Kim, D., Sperber, K., Stern, W., Waliser, D., Kang, I.-S., Maloney, E., Wang, W.,

549   Weickmann, K., Benedict, J., and Khairoutdinov, M.: Application of MJO

550   simulation diagnostics to climate models, Journal of climate, 22, 6413-6436, 2009.

551   Kim, H.-M., Webster, P. J., Toma, V. E., and Kim, D.: Predictability and prediction

552   skill of the MJO in two operational forecasting systems, Journal of Climate, 27,

553   5364-5378, 2014.

554   Klingaman, N. and Woolnough, S.: The role of air–sea coupling in the simulation of the

555   Madden–Julian oscillation in the Hadley Centre model, Quarterly Journal of the

556   Royal Meteorological Society, 2013.

557   Klingaman, N. P. and Demott, C. A.: Mean state biases and interannual variability

558   affect perceived sensitivities of the Madden-Julian Oscillation to air-sea coupling,

559   Journal of Advances in Modeling Earth Systems, 12, e2019MS001799, 2020.

560   Krishnamurti, T. N., Oosterhof, D., and Mehta, A.: Air–sea interaction on the time scale

561   of 30 to 50 days, Journal of the atmospheric sciences, 45, 1304-1322, 1988.

562   Lan, Y.-Y., Tsuang, B.-J., Tu, C.-Y., Wu, T.-Y., Chen, Y.-L., and Hsieh, C.-I.:

563   Observation and simulation of meteorology and surface energy components over

564   the South China Sea in summers of 2004 and 2006, Terrestrial, Atmospheric and

565   Oceanic Sciences, 21, 325-342, 2010.

566   Lan, Y. Y., Hsu, H. H., Tseng, W. L., and Jiang, L. C.: Embedding a One-column

567   Ocean Model (SIT 1.06) in the Community Atmosphere Model 5.3 (CAM5.3;

568   CAM5–SIT v1.0) to Improve Madden–Julian Oscillation Simulation in Boreal

569   Winter, Geosci. Model Dev. Discuss., 2021, 1-49, 10.5194/gmd-2021-346, 2021.

570   Li, Y. and Carbone, R. E.: Excitation of Rainfall over the Tropical Western Pacific,

571   Journal of the Atmospheric Sciences, 69, 2983-2994, 10.1175/jas-d-11-0245.1,

572   2012.

573   Liebmann, B.: Description of a complete (interpolated) outgoing longwave radiation

574   dataset, Bull. Amer. Meteor. Soc., 77, 1275-1277, 1996.

575   Madden, R. A. and Julian, P. R.: Description of global-scale circulation cells in the

576   tropics with a 40-50 day period, J. atmos. Sci, 29, 1109-1123, 1972.

577   Marshall, A. G., Alves, O., and Hendon, H. H.: An Enhanced Moisture Convergence–

578   Evaporation Feedback Mechanism for MJO Air–Sea Interaction, Journal of the

579   Atmospheric Sciences, 65, 970-986, 10.1175/2007jas2313.1, 2008.

580   Matthews, A. J., Singhruck, P., and Heywood, K. J.: Deep ocean impact of a Madden-

581   Julian Oscillation observed by Argo floats, Science, 318, 1765-1769, 2007.

582   Matthews, A. J., Baranowski, D. B., Heywood, K. J., Flatau, P. J., and Schmidtko, S.:

583   The surface diurnal warm layer in the Indian Ocean during CINDY/DYNAMO,

584   Journal of Climate, 27, 9101-9122, 2014.

585   McPhaden, M. J., Busalacchi, A. J., and Anderson, D. L.: A toga retrospective,

586   Oceanography, 23, 86-103, 2010.

587   Mellor, G. L. and Yamada, T.: Development of a turbulence closure model for

588   geophysical fluid problems, Reviews of Geophysics, 20, 851-875, 1982.

589   Nordeng, T. E.: Extended versions of the convective parametrization scheme at

590   ECMWF and their impact on the mean and transient activity of the model in the

591   tropics, European Centre for Medium-Range Weather Forecasts1994.

592   Oliver, E. and Thompson, K.: Sea level and circulation variability of the Gulf of

593   Carpentaria: Influence of the Madden-Julian Oscillation and the adjacent deep

594   ocean, Journal of Geophysical Research: Oceans, 116, 2011.

595   Park, S. and Bretherton, C. S.: The University of Washington shallow convection and

596   moist turbulence schemes and their impact on climate simulations with the

597   Community Atmosphere Model, Journal of Climate, 22, 3449-3469, 2009.

598   Roeckner, E.: The atmospheric general circulation model ECHAM5: Part 1: model

599   description, Max-Planck-Institut fuer Meteorologie2003.

600   Roeckner, E., Brokopf, R., Esch, M., Giorgetta, M., Hagemann, S., Kornblueh, L.,

601   Manzini, E., Schlese, U., and Schulzweida, U.: Sensitivity of simulated climate to

602   horizontal and vertical resolution in the ECHAM5 atmosphere model, Journal of

603   Climate, 19, 3771-3791, 2006.

604   Salby, M. L. and Hendon, H. H.: Intraseasonal behavior of clouds, temperature, and

605   motion in the tropics, Journal of the Atmospheric Sciences, 51, 2207-2224, 1994.

606   Shinoda, T. and Hendon, H. H.: Mixed layer modeling of intraseasonal variability in the

607   tropical western Pacific and Indian Oceans, Journal of Climate, 11, 2668-2685,

608   1998.

609   Sobel, A. H., Maloney, E. D., Bellon, G., and Frierson, D. M.: The role of surface heat

610   fluxes in tropical intraseasonal oscillations, Nature Geoscience, 1, 653-657, 2008.

611   Sobel, A. H., Maloney, E. D., Bellon, G., and Frierson, D. M.: Surface fluxes and

612   tropical intraseasonal variability: A reassessment, Journal of Advances in

613   Modeling Earth Systems, 2, 2010.

614   Team, G. G. A. M. D., Anderson, J. L., Balaji, V., Broccoli, A. J., Cooke, W. F.,

615   Delworth, T. L., Dixon, K. W., Donner, L. J., Dunne, K. A., and Freidenreich, S.

616   M.: The new GFDL global atmosphere and land model AM2–LM2: Evaluation

617   with prescribed SST simulations, Journal of Climate, 17, 4641-4673, 2004.

618   Tseng, W.-L., Tsuang, B.-J., Keenlyside, N., Hsu, H.-H., and Tu, C.-Y.: Resolving the

619   upper-ocean warm layer improves the simulation of the Madden–Julian oscillation,

620   Climate Dynamics, 1-17, 10.1007/s00382-014-2315-1, 2015.

621   Tsuang, B.-J., Tu, C.-Y., and Arpe, K.: Lake parameterization for climate models.,

622   Max-Planck-Institute for Meteorology Rept, 316, 72pp, 2001.

623   Tsuang, B.-J., Tu, C.-Y., Tsai, J.-L., Dracup, J. A., Arpe, K., and Meyers, T.: A more

624   accurate scheme for calculating Earths-skin temperature, Climate Dynamics, 32,

625   251-272, 2009.

626   Tu, C.-Y.: Sea Surfce Temperature Simulation in Climate Model, Department of

627   Environmental Engineering, National Chung Hsing University, 2006.

628   Tu, C.-Y. and Tsuang, B.-J.: Cool-skin simulation by a one-column ocean model,

629   Geophysical research letters, 32, 2005.

630   Tu, C.-Y. and Tsuang, B.-J.: Numerical discretization for sea surface temperature

631   simulation in a turbulent kinetic energy ocean model, 2014.

632   Wang, B. and Rui, H.: Dynamics of the Coupled Moist Kelvin-Rossby Wave on an

633   Equatorial-Plane, Journal of the Atmospheric Sciences, 47, 397-413, 1990.

634   Wang, B. and Xie, X.: Coupled modes of the warm pool climate system. Part I: The role

635   of air–sea interaction in maintaining Madden–Julian oscillation, Journal of

636   Climate, 11, 2116-2135, 1998.

637   Wang, G., Ling, Z., Wu, R., and Chen, C.: Impacts of the Madden–Julian oscillation on

638   the summer South China Sea ocean circulation and temperature, Journal of climate,

639   26, 8084-8096, 2013.

640   Watterson, I. and Syktus, J.: The influence of air–sea interaction on the Madden–Julian

641   oscillation: The role of the seasonal mean state, Climate dynamics, 28, 703-722,

642   2007.

643   Webber, B. G., Matthews, A. J., and Heywood, K. J.: A dynamical ocean feedback

644   mechanism for the Madden–Julian oscillation, Quarterly Journal of the Royal

645   Meteorological Society: A journal of the atmospheric sciences, applied

646   meteorology and physical oceanography, 136, 740-754, 2010.

647   Webber, B. G., Matthews, A. J., Heywood, K. J., and Stevens, D. P.: Ocean Rossby

648   waves as a triggering mechanism for primary Madden–Julian events, Quarterly

649   Journal of the Royal Meteorological Society, 138, 514-527, 2012.

650   Wheeler, M. C. and Hendon, H. H.: An all-season real-time multivariate MJO index:

651   Development of an index for monitoring and prediction, Monthly Weather Review,

652   132, 1917-1932, 2004.

653   Woolnough, S. J., Slingo, J. M., and Hoskins, B. J.: The relationship between

654   convection and sea surface temperature on intraseasonal timescales, Journal of

655   Climate, 13, 2086-2104, 2000.

656   Zhang, C.: Madden-Julian oscillation, Reviews of Geophysics, 43, 2005.

657   Zhang, G. J. and McFarlane, N. A.: Sensitivity of climate simulations to the

658   parameterization of cumulus convection in the Canadian Climate Centre general

659   circulation model, Atmosphere-ocean, 33, 407-446, 1995.

660   Zhao, M., Held, I. M., Lin, S.-J., and Vecchi, G. A.: Simulations of global hurricane

661   climatology, interannual variability, and response to global warming using a 50-km

662   resolution GCM, Journal of Climate, 22, 6653-6678, 2009.

663

	ECHAM5-SIT	CAM5-SIT	HiRAM-SIT
AGCM	ECHAM5	CAM5	HiRAM
Horizontal resolution	T63(~2°)	1.9°×2.5°	1°×1°
BC — SST	OISST	OISST	OISST
BC — SIC	OISST	OISST	OISST
BC — OT/OS	GODAS	GODAS	GODAS
Atmosphere vertical resolution	L31	L30	L32
Ocean vertical resolution	42	42	42
Coupled region	30˚S–30˚N	30˚S–30˚N	30˚S–30˚N
Time	1985–2005 (21 years)		

664

665 **Table 1.** Detailed information of models and experiments

666

667
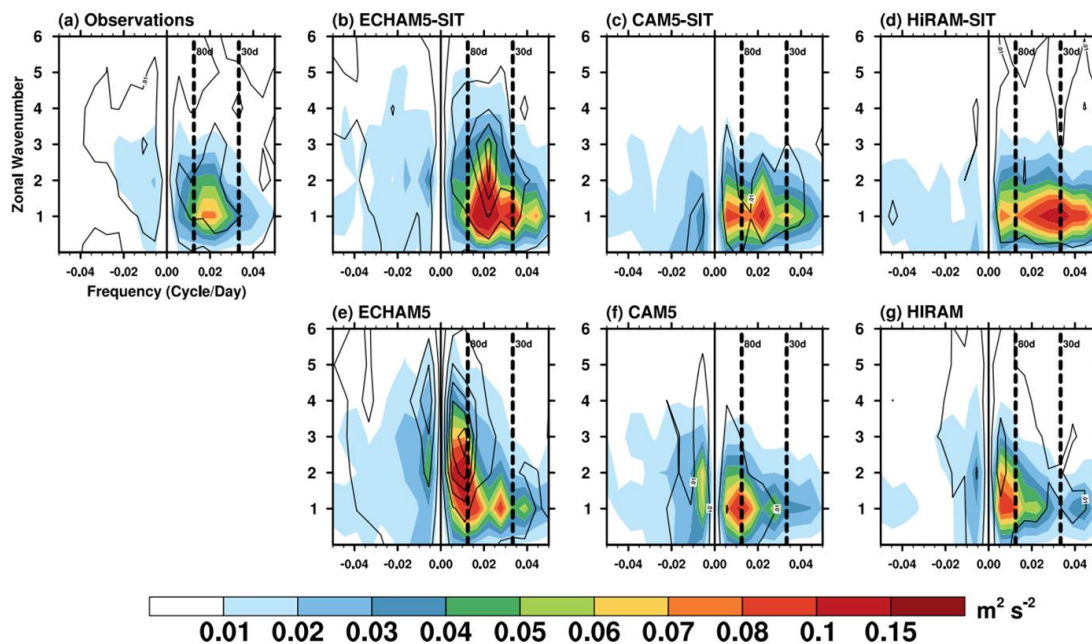
Figure 1. Wavenumber–frequency spectra for equatorial 850-hPa zonal wind (shading;

m^2 s^{-2}) and precipitation (contours; mm^2 day^{-2}) over 10°S–10°N from (a) observations

and simulations using the (b–d) coupled and (e–g) uncoupled AGCM.

672

673

674
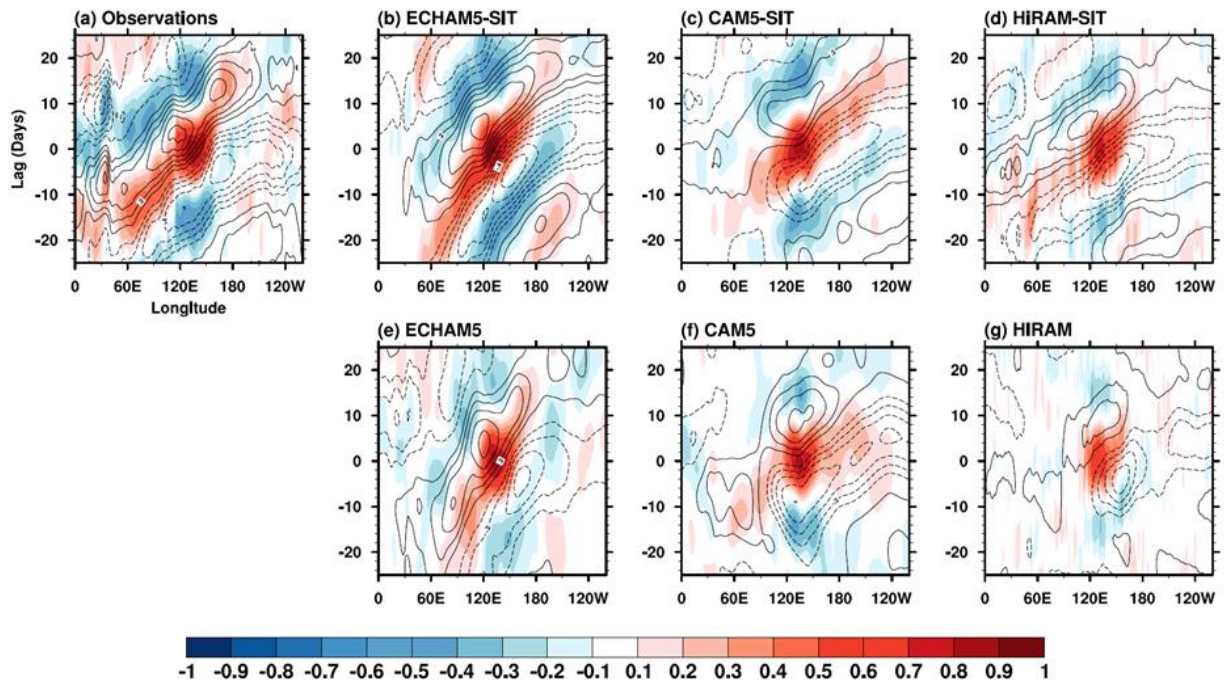
Figure 2. 10°S–10°N averaged lag–longitude diagrams of intraseasonal precipitation (shading) and 10-m zonal wind (contour) correlated against precipitation at region (10°S–5°N, 120°E–150°E) from (a) observations and simulations using the (b–d) coupled and (e–g) uncoupled AGCM. The contour interval is 0.1.
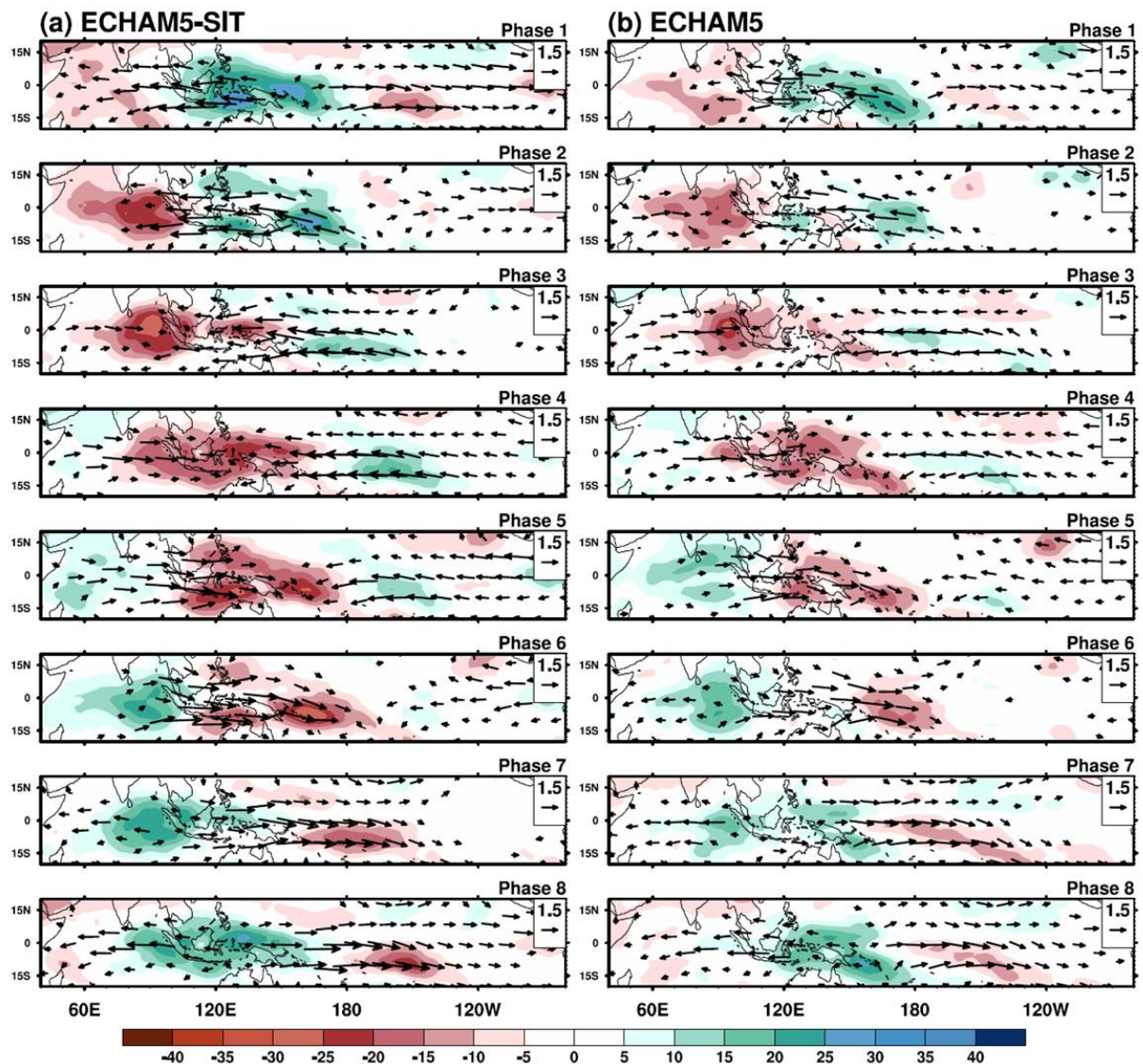
679
680   **Figure 3.** Composite November–April 20–100-day OLR (W m⁻¹; color) and 10-m surface

681   wind anomalies (m s⁻¹; vectors) as a function of the MJO phase in (a) ECHAM5-SIT and

682   (b) ECHAM5. Vectors <0.6 m s⁻¹ are not shown. The reference vector in units of m s⁻¹ is

683   shown at the bottom right. The number of days used to generate the composite for each

684   phase is shown to the right of each panel.

685
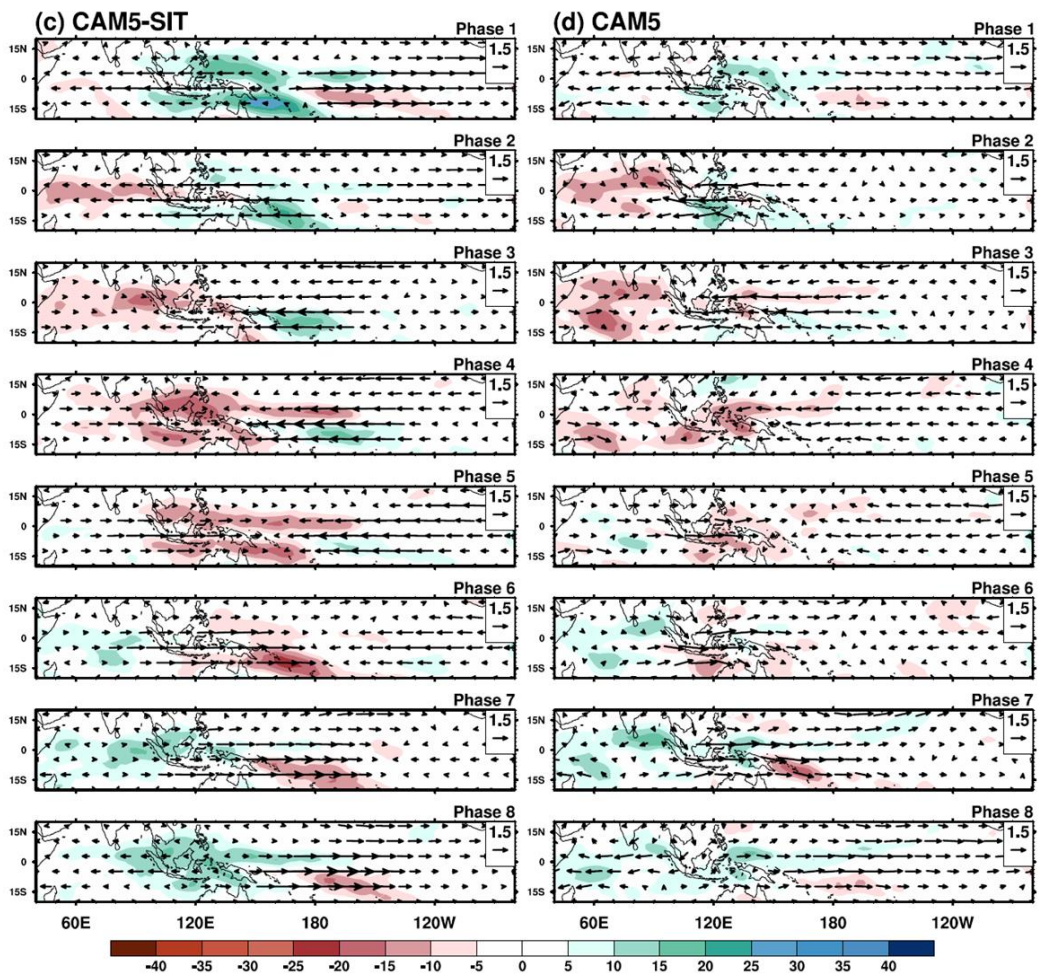
Figure 3. continued, (c) CAM5-SIT and (d) CAM5.
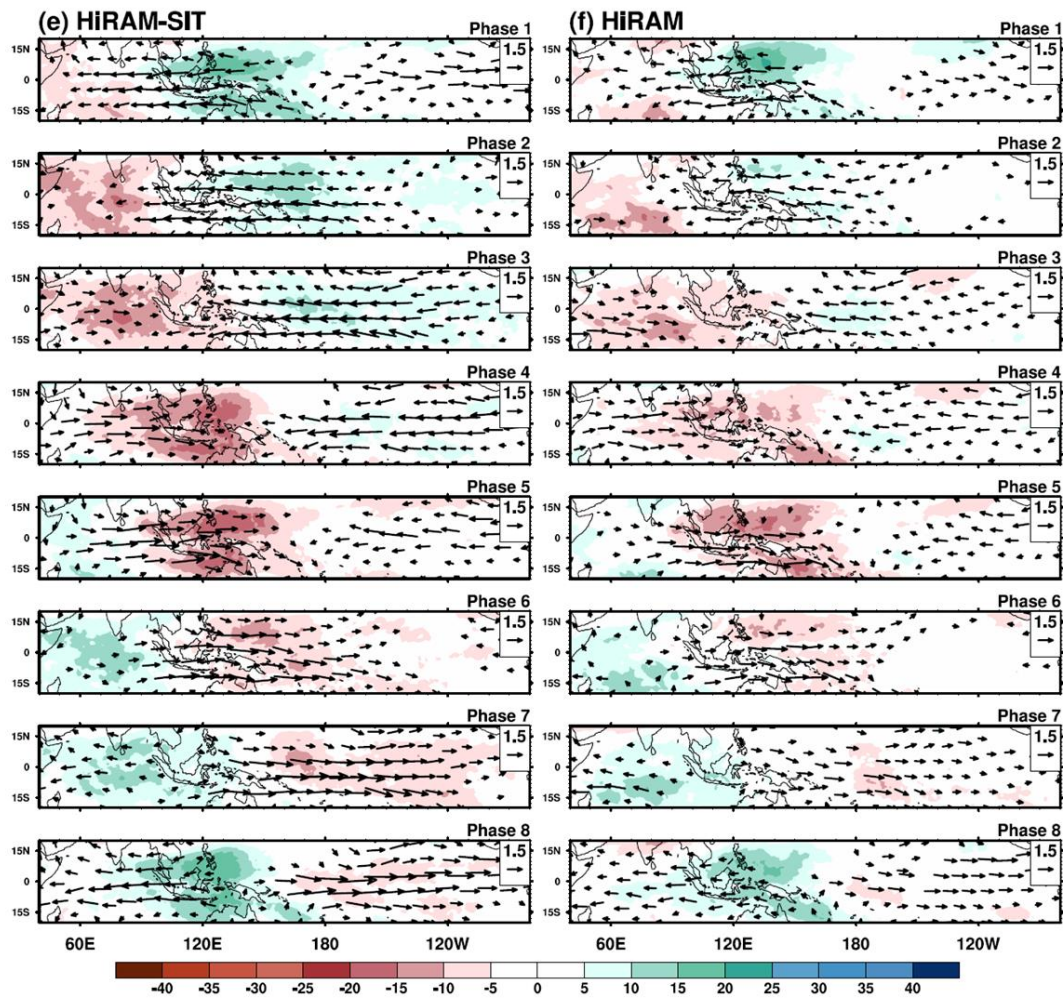
Figure 3. continued, (e) HiRAM-SIT and (f) HiRAM.
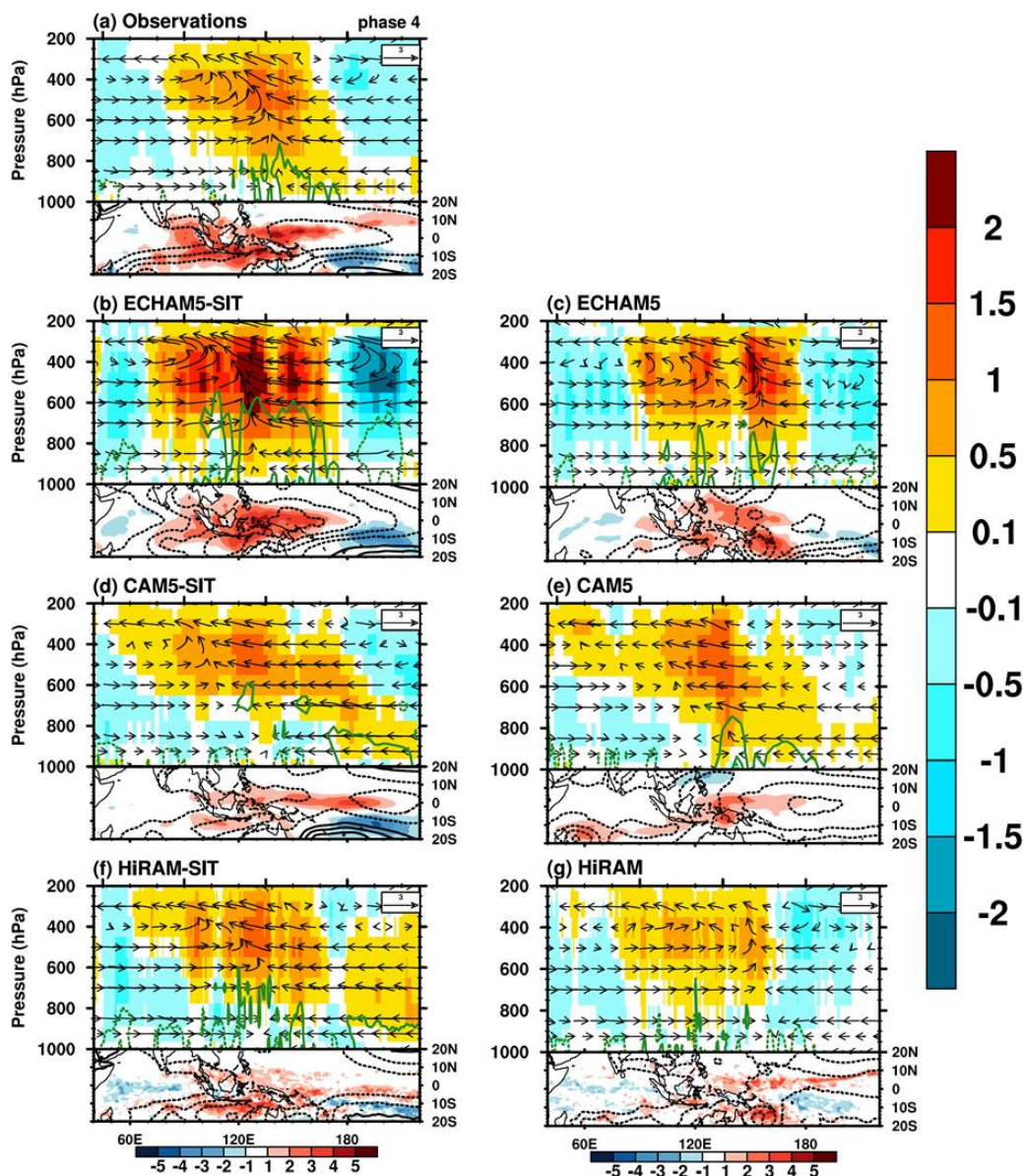
Figure 4. Structure of simulated MJO in phase 4. The longitude–height cross-sections (averaged over 10°S–EQ) of the MJO scaled wind circulation (vector, u: m s^{-1}, omega: 10^{-2} Pa s^{-1}), Q1 (shading, unit: K day^{-1}), and the horizontal moisture convergence (green contour, unit: 10^{-6} g kg^{-1} s^{-1}) from (a) observations and simulations using the (b–d) coupled and (e–g) uncoupled AGCMs. The contour interval of the moisture convergence is 8 × 10^{-6} g kg^{-1} s^{-1}; solid line is positive. Precipitation (shading, unit: mm day^{-1}) and

700   sea level pressure (contour, unit: hPa). Contour interval of sea level pressure is 30 hPa;

701   dashed line indicates negative.

702
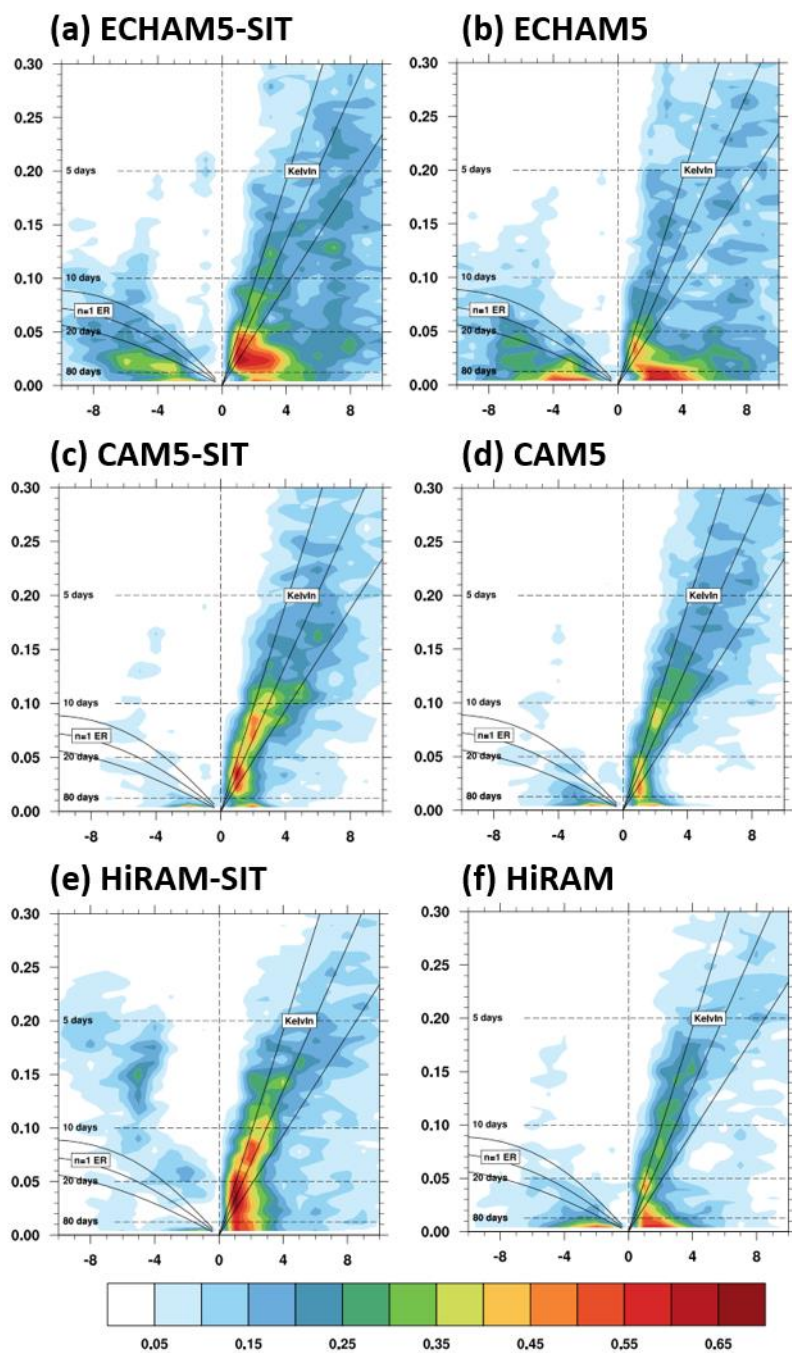
Figure 5. Symmetric wavenumber–frequency spectra of 10°N–10°S-averaged 850-hPa zonal wind using the (a, c, e) coupled and (b, d, f) uncoupled AGCMs. Units: $m^2\ s^{-2}$.
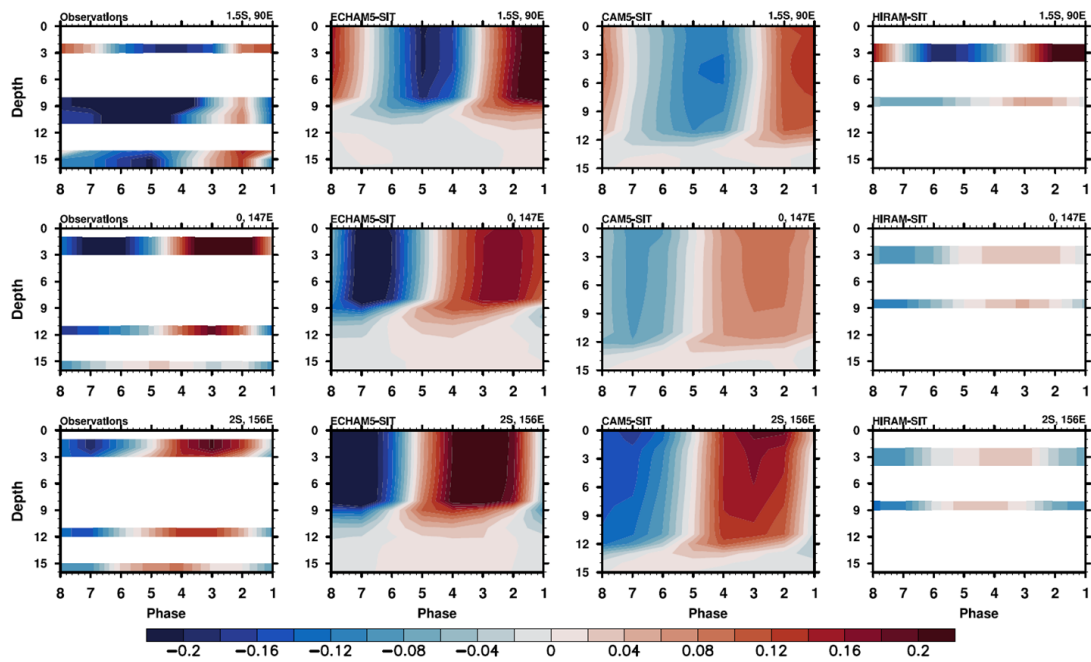
Figure 6. Vertical ocean temperature (°C) profiles with respect to MJO phases for intraseasonal anomalies (i.e., with 20–100-day filtering) in observations and simulations using coupled models. Observations are in suit with data from TAO. Because of storage limitations, only 3 and 10 m water temperatures are presented in the HiRAM-SIT simulation.

42
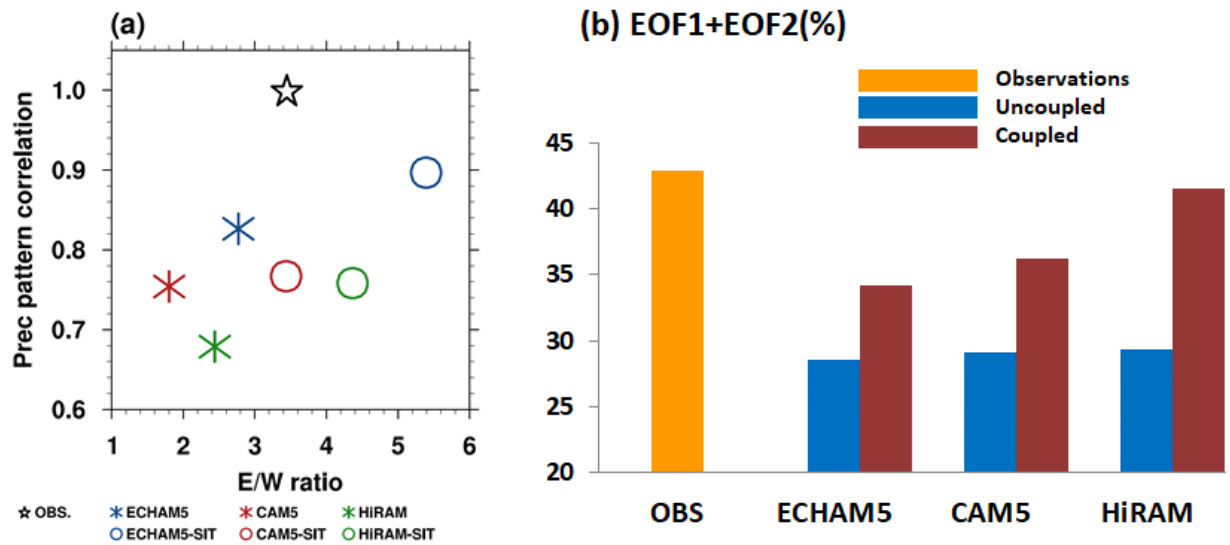
Figure 7. Scatter plots of various MJO indices based on observation and experiments (Table 1). (a) X-axis is the power ratio of east–west propagating waves. The east–west ratio was calculated by dividing the sum eastward-propagating power by the westward-propagating counterpart within wavenumbers 1–3 (1–2 for zonal wind), period 30–80 days. Y-axis is the pattern correlation of precipitation eastward propagation, as shown in Fig. 2. (b) Sum of RMM1 and RMM2 variances based on Wheeler and Hendon (2004).

42
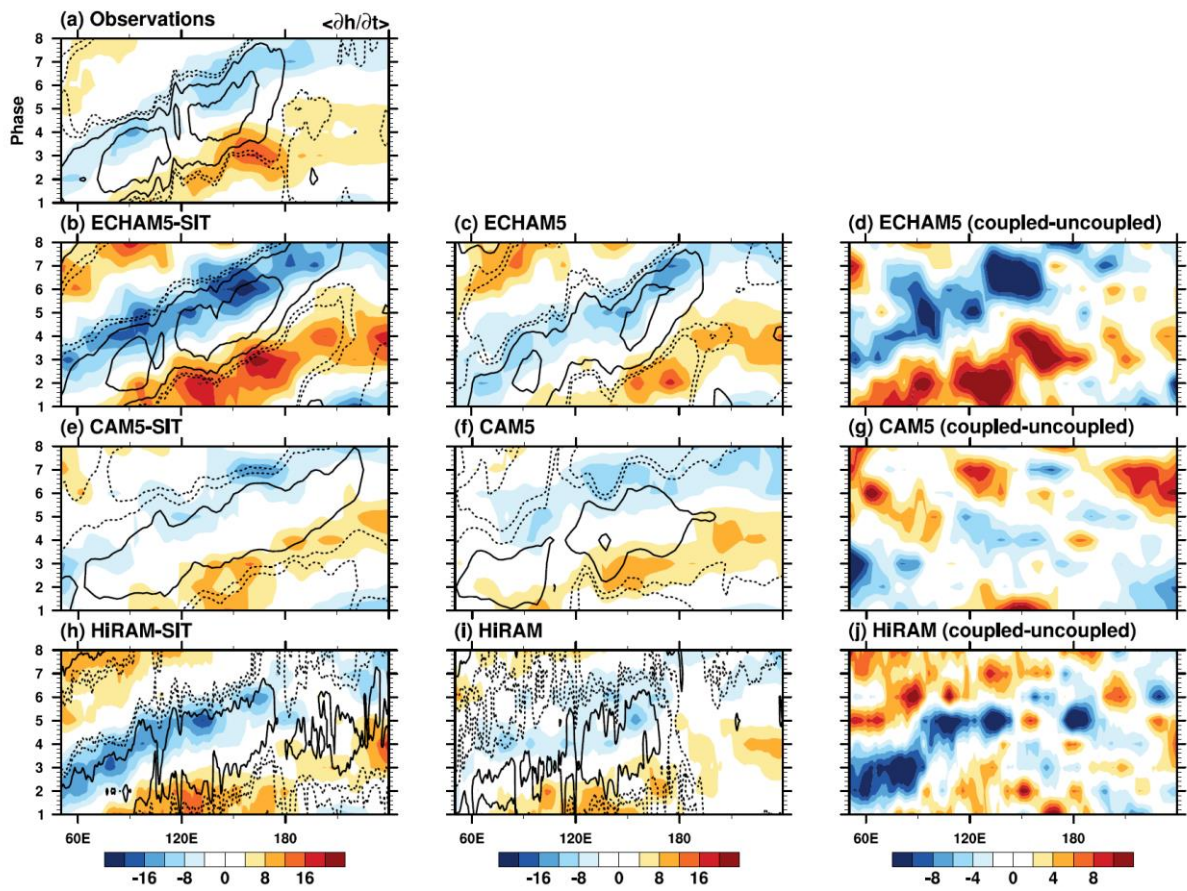
Figure 8. 10°S–EQ averaged Hovmöller diagrams of MSE (shading; J kg^{-1}) and precipitation (contour; mm day^{-1}) composite followed the RMM index from (a) observations and simulations using the (b, e, j) coupled and (c, f, k) uncoupled AGCMs and (d, i, l) their difference. The contour interval is precipitation anomalies.
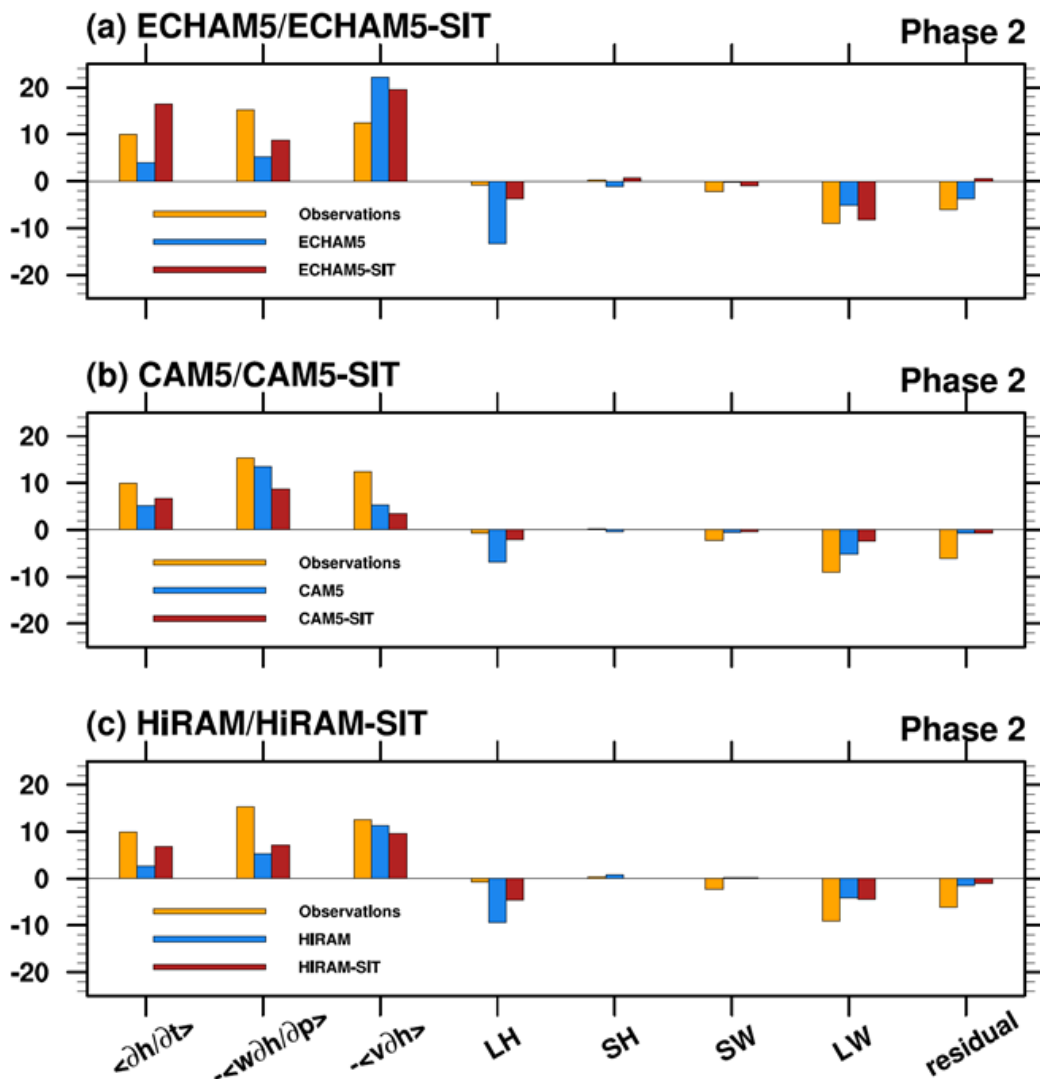
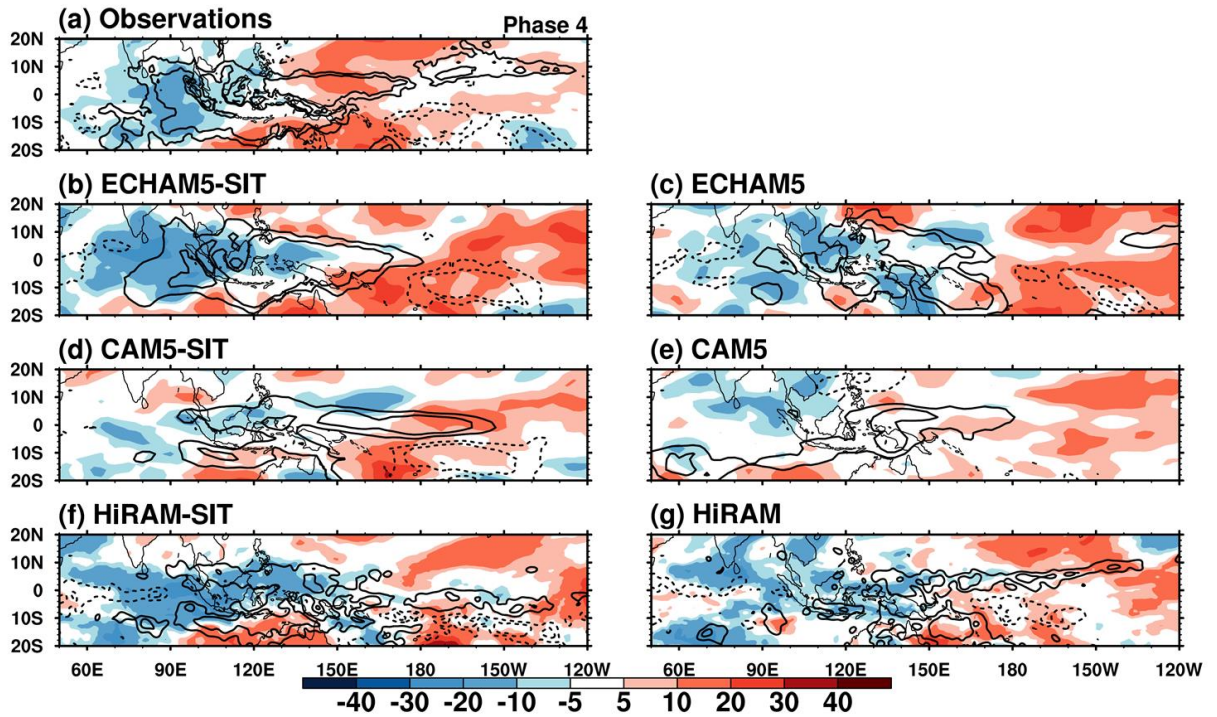**Figure 9.** Model-simulated column-integrated MSE budget terms (J kg^{-1} s^{-1}) during

phase 2 of the MJO. Black, red, and blue represents the data from the observations,

Nordeng scheme simulation, and Tiedtke scheme simulation, respectively. The averaged
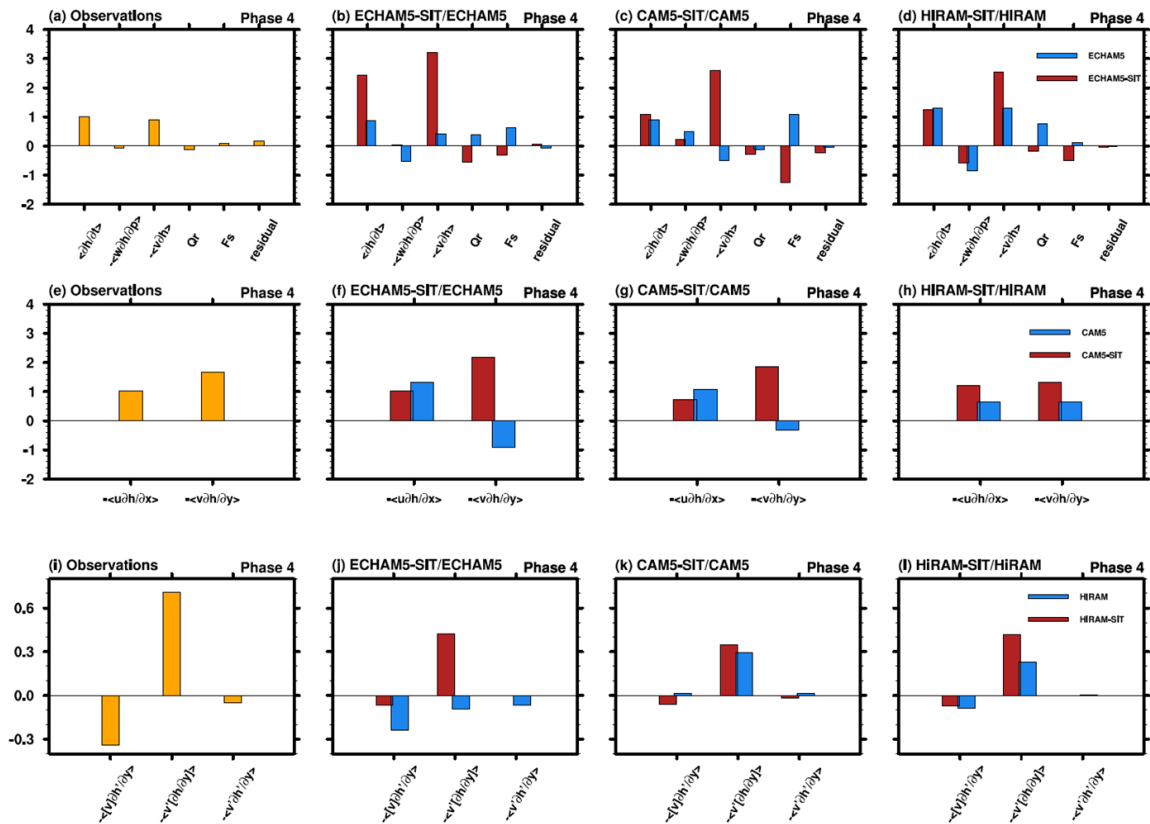
domain is 10°S–EQ and 120°–150°E.

738

739

Figure 10. Phase 4 of the column-integrated MSE tendency (shading; J kg^{-1} s^{-1}) and

precipitation (contours; mm day^{-1}) based on (a) observation, (b) ECHAM5-SIT, (c)

ECHAM5, (d) CAM5-SIT, (e) CAM5, (g) HiRAM-SIT, and (f) HiRAM. The nine-point

local smoothing is applied in the intraseasonal precipitation variance of HiRAM here

(contours only).

745

746

747

748

**Figure 11.** (a–d) Relative role of each MSE component of phase 4 through the projection

of the spatial pattern of each MSE budget over the MC (domain) onto the total MSE

tendency pattern (Fig. 8a). (e–h) Decomposite of the total horizontal MSE advection

based on zonal and meridional components. (i–l) Decomposite of the meridional

horizontal MSE advection based on the MJO circulation and the mean state of moisture.

754
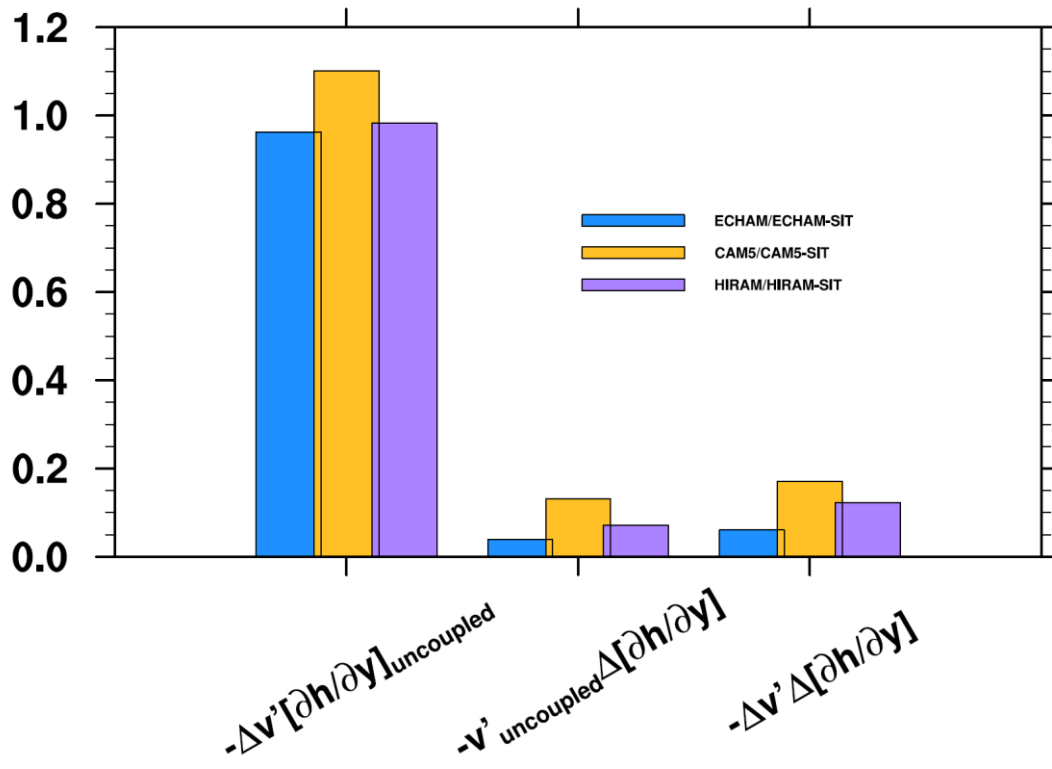
Figure 12. Bar chart of relative contribution of intraseasonal convergence and background moisture between the coupled and uncoupled changes in MJO phase 4.